RSC Advances

PAPER

View Article Online
View Journal | View Issue

Cite this: *RSC Adv.*, 2023, **13**, 21962

Porous nanorods by stacked NiO nanoparticulate exhibiting corn-like structure for sustainable environmental and energy applications†

Vishesh Manjunath, [a] Santosh Bimli, [a] Diwakar Singh,[a] Rathindranath Biswas, [b] Pravin N. Didwal,[cd] Krishna Kanta Haldar, [b] Nishad G. Deshpande,[e] Preeti A. Bhobe [f] and Rupesh S. Devan *[ag]

A porous 1D nanostructure provides much shorter electron transport pathways, thereby helping to improve the life cycle of the device and overcome poor ionic and electronic conductivity, interfacial impedance between electrode–electrolyte interface, and low volumetric energy density. In view of this, we report on the feasibility of 1D porous NiO nanorods comprising interlocked NiO nanoparticles as an active electrode for capturing greenhouse CO_2, effective supercapacitors, and efficient electrocatalytic water-splitting applications. The nanorods with a size less than 100 nm were formed by stacking cubic crystalline NiO nanoparticles with dimensions less than 10 nm, providing the necessary porosity. The existence of Ni^{2+} and its octahedral coordination with O^{2-} is corroborated by XPS and EXAFS. The SAXS profile and BET analysis showed 84.731 m^2 g^{-1} surface area for the porous NiO nanorods. The NiO nanorods provided significant surface-area and the active-surface-sites thus yielded a CO_2 uptake of 63 mmol g^{-1} at 273 K *via* physisorption, a specific-capacitance (C_S) of 368 F g^{-1}, along with a retention of 76.84% after 2500 cycles, and worthy electrocatalytic water splitting with an overpotential of 345 and 441 mV for HER and OER activities, respectively. Therefore, the porous 1D NiO as an active electrode shows multifunctionality toward sustainable environmental and energy applications.

Received 14th May 2023
Accepted 4th July 2023

DOI: 10.1039/d3ra03209d

rsc.li/rsc-advances

Introduction

The use of multifunctional materials in energy generation, energy storage, and CO_2 capture shall address the global energy crises and environmental pollution. However, finding functional materials for multiple applications is necessary to address these issues. Among all the available functional materials, metal oxides render various unique properties due to their completely and partially filled 's' and 'd' orbitals, respectively.[1] Owing to the unique properties like wide bandgaps,[2] high dielectric constants,[3] and tunable optoelectronic characteristics,[4] the metal oxides are applied in different functional applications, such as solar cells,[5,6] photodetectors,[7,8] supercapacitors,[9] battery electrodes,[10] gas sensors,[11] and electrochromism.[12] Moreover, the metal oxides can be downscaled into nanostructures with different shapes and morphologies, providing an increased surface-to-volume ratio and significantly larger textural boundaries.[13] Currently, layered, nanoparticulate, and mesoporous structures have gained considerable attention from researchers to gain enhanced chemical and physical properties. However, such structures compromise the conductivity and electron/ion transport/diffusion owing to the larger charge transfer resistance. Therefore, the synthesis of highly porous oriented structures of interconnecting nanoparticles with larger surface area is of scientific importance. The porous 1D nanostructure morphologies are anticipated to offer fast charge transport in the axial direction, benefiting nanodevice and nanoelectronic applications.[14] Therefore, porous 1D metal oxide nanostructures with high-aspect-ratio and substantially large-surface-area are capable of serving in electrocatalysis, carbon dioxide (CO_2) capture, and supercapacitors. Apart from the porous 1D nanostructures, Ru_3Sn_7 with nontrivial topological surface states recently exhibited superior HER activity to Ru, Pt/C in a wide pH range.[15] The use of metal nanocatalysts has shown promise towards both hydrogen

[a]*Department of Metallurgical Engineering and Materials Science, Indian Institute of Technology Indore, Khandwa Road, Simrol, Indore, 453552, India. E-mail: rupesh@iiti.ac.in*

[b]*Department of Chemistry, Central University of Punjab, Bathinda, 151001, India*

[c]*Department of Materials, University of Oxford, Parks Road, Oxford, OX1 3PH, UK*

[d]*Department of Materials Science and Engineering, Chonnam National University, 77, Yongbongro, Buk-gu, Gwangju, 61186, South Korea*

[e]*Indian Institute of Information Technology, Surat, Kholvad Campus, Kamrej, Surat, 394190, India*

[f]*Department of Physics, Indian Institute of Technology Indore, Khandwa Road, Simrol, Indore, 453552, India*

[g]*Centre for Electric Vehicle & Intelligent Transport Systems, Indian Institute of Technology Indore, Khandwa Road, Simrol, Indore, 453552, India*

† Electronic supplementary information (ESI) available. See DOI: https://doi.org/10.1039/d3ra03209d

evolution reactions (HER) and oxygen evolution reactions (OER) activities.[16] The heterogeneous interface between the Ir nanoclusters and IrO_2 benefitted from the newly-formed active surfaces, and the oxygen vacancies-rich surfaces resulted in an overpotential of 329 mV at 10 mA cm^{-2} towards OER activity.[17] The IrO_2 catalyst dispersed over the porous TiN layer formed over Ti sheets by nitriding showed a better overpotential (302 mV) than the IrO_2 directly dispersed over Ti sheets to achieve a similar current density (J).[18]

Among the metal oxides, nickel oxide is capable of existing in NiO, NiO_2, and Ni_2O_3 forms with cubic, monoclinic, rhombohedral, and/or hexagonal crystalline phases,[1] and is an excellent candidate for a variety of applications. Therefore, the thin-films and nanomaterials of NiO, which can be found to have morphologies like nanospheres,[19] nanoflakes,[20] nanotubes,[21] nanofibers,[22] and pinecones,[23] are independently explored for applications in energy storage, sensors, photocatalysis, and other applications. The hydrothermally synthesized NiO nanoflakes and urchinlike nanostructures,[24,25] 2D nanoflakes and 1D nanorods of NiO obtained by decomposition of $NiC_2O_4 \cdot 2H_2O$,[26] and NiO nanorods grown over Ni foil by calcinating Ni foil dipped in LiOH[27] described the potentials of 1D nanostructures in stable energy storage performance, but their specific capacitance (C_S) was limited to 140 to 290 F g^{-1}. On the contrary, the NiO microflower of particulate nanowire-weaving nanosheets[28] and metal–organic frameworks derived mesoporous NiO nanorod[29] performed well for electrochemical charge storage and demonstrated the necessity of porous 1D morphology, providing a larger surface area accounting for enhanced C_S. Moreover, the NiO nanostructures are explored for electrocatalytic water-splitting processes owing to the co-existence of Ni^{2+}, as well as Ni^{3+} ions. NiO hollow spheres, offering a larger surface area, provide the overall water spitting at an overpotential of 424 and 370 mV for HER and OER activity at the J of 10 mA cm^{-2}.[30] The introduction of reduced graphene oxide (rGO) in the Ni/NiO nanostructures delivered O_2 and H_2 evolution at an overpotential of 480 and 582 mV, respectively.[31] However, the synthesized NiO nanoparticle/graphene oxide composite[32] and Ni–NiO@3Dgraphene composites[33] could not serve the purpose of excellent water splitting, and restricted further improvement with the overpotentials of 453 and 625 mV, and 1640 and 310 mV, respectively, for OER and HER. Nevertheless, MoS_2@NiO nanocomposites provided a relatively better overpotential of 406 mV; the water splitting was limited to the HER only.[34] The combination of Ni_2P and Ni_3P obtained by electroless plating followed by calcination at 300 °C demonstrates fast charge kinetics, yielding an overpotential of 65 mV at J of 10 mA cm^{-2}.[35] Therefore, synthesizing porous NiO nanostructures that deliver a higher surface area for abundant electrocatalytic active sites and enhanced charge conductivity would be beneficial toward achieving improved water-splitting performance. However, most of the porous nanostructures are tailored using a sacrificial template during synthesis, in which the obtained nanostructures are probed for a single application. Thus, the porous nanostructures are expected to grow depending on the structure of the sacrificial template. Contrarily, engineering aligned porous nanostructures consisting of interconnected nanoparticles without employing sacrificial templates using the facile hydrothermal technique is expected to deliver multifunctional properties that can provide applications in energy storage, hydrogen fuel generation, CO_2 capture, *etc.*

In light of the above discussions, in our previous investigations, we studied the effect of morphology and porosity of 0D and 2D NiO on water electrolysis. The 0D NiO nanoparticle morphology performed better compared to that of 2D nanoplates.[36] Therefore, in this study, 1D NiO nanorods comprising interlocked NiO nanoparticles were synthesized by the hydrothermal method. The as-synthesized NiO nanorods were comprehensively characterized to understand the crystallinity, morphology, porosity, chemical states, and local chemical environment. Furthermore, in an attempt to understand the multifunctional property of the synthesized NiO nanorods for sustainable energy applications, the nanorods were employed as a catalyst for greenhouse CO_2 capture, an electrode for supercapacitor, and an electrocatalyst for water splitting to generate hydrogen fuel. Interestingly, the porous NiO nanorods formed by interconnecting nanoparticles showed good CO_2 uptake, energy storage performance, and low overpotential for OER and HER. Additionally, the NiO nanorods as an electrode for supercapacitors and electrocatalysts for water-splitting showed capacitance retention and stability in acidic and basic media, respectively.

Experimental

The synthesis of porous 1D NiO nanorods formed by stacked NiO particulate was accomplished by hydrothermal reaction for 12 h at 180 °C in a Teflon liner placed in an autoclave. The detailed synthesis procedure is provided in the ESI.† The as-synthesized NiO nanorods were investigated using various characterization techniques to understand the physicochemical properties, such as morphology, crystal structure, and chemical elements. The gas adsorption–desorption measurements were performed to determine the CO_2 uptake in the NiO nanorods. Moreover, the OER and HER activity and energy storage performance of the 1D porous NiO nanorods were evaluated using an electrochemical workstation in the three-electrode configuration. The detailed synthesis procedure and the instruments used for various characterizations are mentioned in the ESI.† The procedure and various equations used for gas adsorption–desorption studies, electrochemical measurements, and electrocatalytic water splitting are thoroughly presented in the ESI† in separate segments.

Results and discussion

From XRD, FESEM, and TEM examination, the crystalline phase and surface-morphological features of NiO were analyzed. The Rietveld refinement was done on the X-ray diffractogram utilizing the FullProf software package to identify the crystal structure and lattice parameter. Fig. 1(a) shows the reflected and analyzed patterns, Bragg's positions, and difference curves for the space group $Fm\bar{3}m$ (ICSD No. 9008693) and $P63/m$ (14-

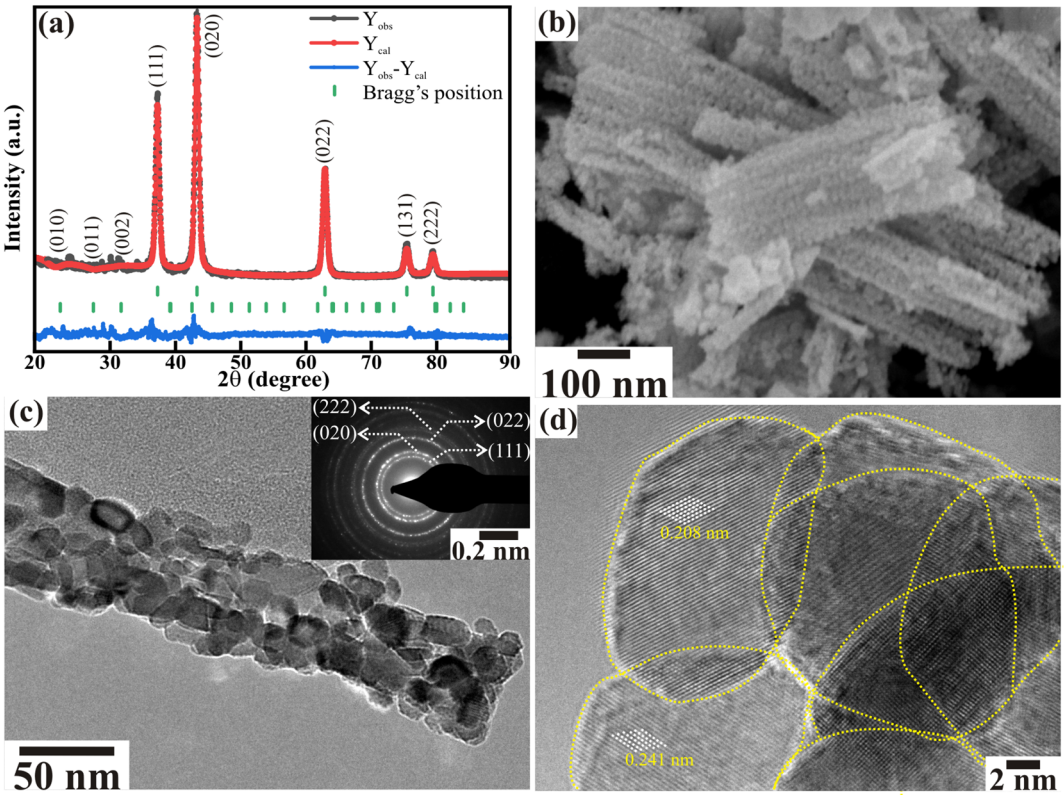

Fig. 1 (a) Rietveld refinement of the XRD pattern (Y_{obs} and Y_{cal} represent the observed and calculated intensity, respectively), (b) FESEM image, (c) TEM image, and (d) HR-TEM image of the NiO nanorods. The inset of (c) represents the SAED pattern of the NiO nanorods. The yellow dotted lines in (d) serve as visual cues to represent the existence of distinct NiO nanoparticles in nanorods.

0481). A reasonably good fit of the diffraction peaks was obtained at $2\theta = 37.33°$, 43.38°, 63.03°, 75.60°, and 79.61°, which correspond to the (111), (020), (022), (131), and (222) peaks, respectively, representing the existence of the cubic NiO phase with a cell volume (V) of 72.68 $cm^3\ g^{-1}$ and lattice parameters (*i.e.*, $a = b = c$) of 4.173 Å. Other minor peaks observed at $2\theta =$ 24.4°, 28.05°, and 31.9° correspond to (010), (011), and (002) crystal planes, indicating the existence of the Ni_2O_3 phase with the cell volume (V) of 102.70 $cm^3\ g^{-1}$ and lattice parameters of 4.585 Å ($\equiv a = b$) and 5.642 Å ($\equiv c$). The values of the fitting parameters, namely R_f (R-factor) and GoF (goodness of fit), are 1.21 and 2.94, respectively. These Rietveld refined results of XRD demonstrate the presence of the NiO (~98.72%) pure phase, along with a minor amount of Ni_2O_3 (~1.28%) in the porous 1D nanorods. The FESEM analysis in Fig. 1(b) represents the formation of porous nanorods with corn-like characteristics along the surface of each rod. Corn-like features are observed due to the regular interconnected assembly of the nanoparticles. Moreover, these interlinked nanoparticles assembled porous NiO nanorods of width < 50 nm. These distinct porous NiO rods are well dispersed with traceable textural boundaries. Profound insights were obtained from TEM analysis, although not revealed to a large extent by FESEM. The TEM image confirmed that the NiO nanorods were formed through the interconnection of randomly aligned distinct NiO nanoparticles (Fig. 1(c)). Moreover, the nanoparticles with clearly visible textural boundaries all have dimensions of <15 nm. The inset of Fig. 1(c) shows discrete circular rings with bright diffraction spots matching the different planes in the SAED pattern of the cubic crystalline NiO nanorods. The HRTEM image revealed the existence of distinct crystalline NiO nanoparticles of dimension ~8 nm with clearly visible textural boundaries identified by yellow lines (Fig. 1(d)). The d-spacings of 0.208 and 0.241 nm correspond to the (020) and (111) planes, respectively, confirming the formation of cubic crystalline NiO nanoparticles, which concurs with the XRD analysis. These analyses confirm the formation of highly crystalline porous NiO nanorods with interlocked NiO nanoparticles.

The electronic states and chemical composition of the porous NiO nanorods were investigated from XPS. The Ni(2p) and O(1s) core levels obtained by deconvoluting the XPS spectra are presented in Fig. 2. The four definite peaks in Fig. 2(a) represent the two peaks of the Ni(2p) core levels and the corresponding shake-up satellites, which are deconvoluted into eight distinct peaks. The $Ni^{2+}(2p_{3/2})$, $Ni^{2+}(2p_{1/2})$, $Ni^{3+}(2p_{3/2})$, and $Ni^{3+}(2p_{1/2})$ peaks are positioned at binding energies of 853.43 ($\equiv a$), 871.48 ($\equiv c$), 855.34 ($\equiv b$), and 873.72 ($\equiv d$), respectively. The peak at binding energies of 860.53 ($\equiv sa$), 865.48 ($\equiv sb$), 878.45 ($\equiv sc$), and 882.89 ($\equiv sd$), on the other hand, denotes their accompanying shake-up satellite peaks. The presence of NiO and Ni_2O_3 phases at the surface is shown by the peaks of $Ni^{3+}(2p_{1/2})$ and $Ni^{2+}(2p_{1/2})$. The deconvolution O(1s) core level

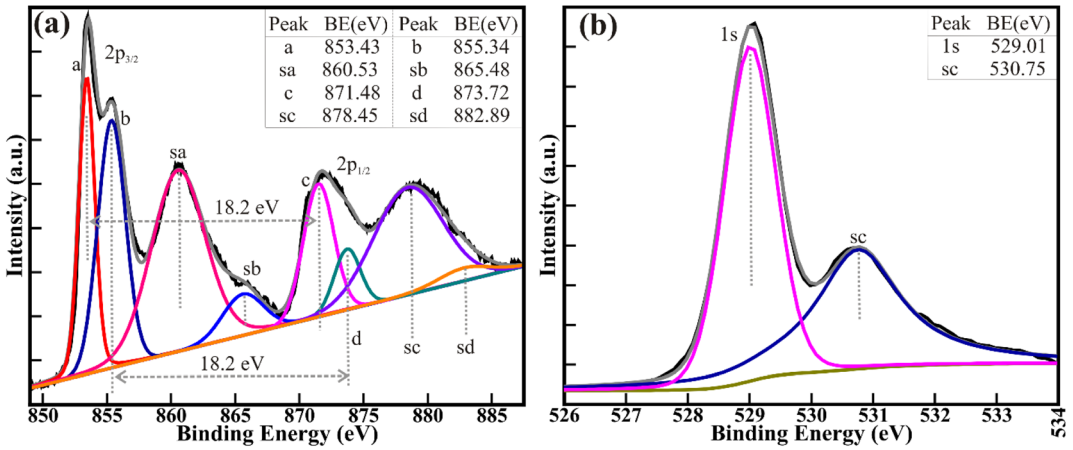

Fig. 2 High-resolution XPS of the (a) Ni(2p) and (b) O(1s) core levels of NiO nanorods. Shirley background and Voigt curve fitting function were used to deconvolute the spectra.

gives two distinct peaks at 529.01 and 530.75 eV, representing the O^{2-} ions and surface defects or contaminants, respectively. Additionally, the gap (eV) between the O(1s) and Ni($2p_{3/2}$) core levels, 324.42 eV, is substantially lower than that between metallic Ni and non-stoichiometric Ni_2O_3 (321.7 eV).[37] Overall, the growth of the stoichiometric NiO nanorods and a small quantity of non-stoichiometric Ni_2O_3 phase described here are supported by the X-ray diffraction analysis. The presence of minute amounts of Ni_2O_3 has positively influenced the ability of porous NiO nanorods to supply multifunctional characteristics.

A tunable X-ray source (lab-based) was used to record the room temperature Ni K-edge absorption spectra in transmission geometry to confirm the oxidation states of Ni ions in porous NiO nanorods. X-ray absorption near-edge structure (XANES) spectra are displayed in Fig. 3. According to Fig. 3(a), NiO nanorods have a Ni^{2+} oxidation state because the absorption-edge shifts apparently towards higher energy than that of regular Ni metal, which also mirrors the typical NiO (Alfa Aesar, 3N) reference sample. Additionally, Fig. 3(b) illustrates a reasonably good fitting to the Fourier-transformed Extended X-ray Absorption Fine Structure (EXAFS) spectrum of the NiO nanorods. The fitting was carried out in the k range of 3–10 $Å^{-1}$ and in the R range of 1–3 Å. Based on the crystal structure information obtained from XRD, a simple model of Ni coordinated to 6 oxygen atoms was developed to fit the EXAFS data.

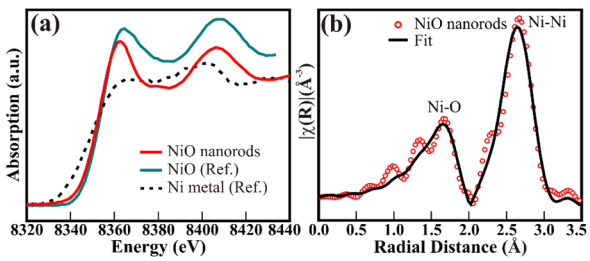

Fig. 3 (a) Nickel K-edge XANES and (b) X-ray absorption fine structure spectra in k-space of the particulate porous NiO nanorods.

Such fitting yields a bond distance of ~2.108 ± 0.015 and a thermal mean square factor of 0.005 ± 0.002.

The size of interlocked nanoparticles in the particulate NiO nanorods is estimated from the fitting/analysis of the SAXS profile collected in the range $2\theta = 0$ to 5° (Fig. 4(a)). The most frequent radius of 6.5 nm corroborates the ~13 nm diameter of the distinct NiO nanoparticles present in the nanorods, offering a porous nature. These interconnecting nanoparticles shaped nanorods of an average radius of 23.56 nm might represent the average diameter of ~47.12 nm for the NiO nanorods. These values of the diameter of nanoparticles and nanorods are akin to those estimated from the FESEM and/or TEM analysis. Nevertheless, confirmed differentiation between the nanoparticles and nanorods from SAXS is challenging in the present case. A substantially greater surface-to-volume ratio (S/V) of 0.0279/Å is the outcome of the nanoscale particles. Furthermore, the porous features were analyzed by N_2 gas adsorption–desorption isotherms at 77 K (Fig. 4(b)). The NiO nanorods showed type IV isotherm (H3 hysteresis), indicating slit-like pores. The BET surface area of 84.731 $m^2\ g^{-1}$ estimated for the particulate porous NiO nanorods is smaller than that for the 0D NiO nanoparticles (106.02 $m^2\ g^{-1}$ for <10 nm size particles) reported in our previous study.[36] This might be due to the stacking or interconnections of the 0D NiO nanoparticles to form the porous 1D NiO nanorods. The analogous BJH pore size distribution of the NiO nanorods (inset of Fig. 4(b)) illustrated the average pore diameter and volume of 3.744 nm and 0.303 $cm^3\ g^{-1}$, respectively. These results strongly complement the values obtained from SAXS analysis and reveal more effective processes, projecting the multifunctionality of the porous NiO nanorods.

The porous NiO nanorods comprising interconnected nanoparticles showed excellent porosity and surface-to-volume ratio, and can therefore be employed for CO_2 capture. The CO_2 uptake of 0.63 and 0.47 mmol g^{-1} was recorded at 273 and 298 K, respectively (Fig. 5(a)). The lower value of CO_2 uptake at higher temperatures (298 K) indicates the exothermic type of adsorption. Therefore, the Clausius–Clapeyron equation was

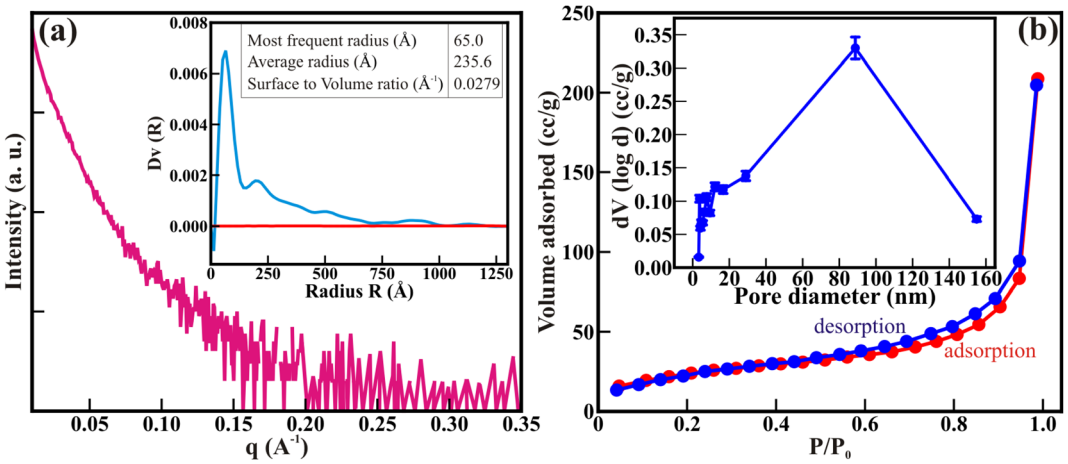

Fig. 4 (a) SAXS profile of the particulate NiO nanorods; the inset shows corresponding best fitting/analysis using Easy-SAXS software. (b) Adsorption–desorption (N_2) isotherm and distribution of the BJH pore diameters (in the inset) of the particulate porous NiO nanorods.

used to compute the isosteric heat of CO_2 adsorption ($-Q_{st}$), which was then used to determine the nature of CO_2 adsorption on the NiO nanorods (Fig. 5(b)). The $-Q_{st}$ values in the range of 8.53 kJ mol^{-1} to 7.41 kJ mol^{-1} indicates the physisorption of CO_2 gas over porous NiO nanorod surface, which also shows the ease of regeneration of the NiO nanorods. Moreover, the $-Q_{st}$ values dropped as the CO_2 uptake increased, showing that the active interaction sites were saturated with higher CO_2 loading.

Owing to the high porosity in the NiO nanorods obtained due to the interconnected nanoparticles, the electrochemical energy storage performance is evaluated from CV and GCD analysis (Fig. 6). The reversible redox peaks derived from the Ni^{2+}/Ni^{3+} redox couples during charging (*i.e.*, oxidation) and discharging (*i.e.*, reduction) are observed for the CV curves obtained at various scanning rates from 5 to 100 mV s^{-1} at an applied potential in the range of 0.1 to 0.6 V (*vs.* SCE/V) (Fig. 6(a)). These Ni^{2+}/Ni^{3+} redox couples assist in the diffusion and extraction of OH^- ions from the surface of nanoparticles in the NiO nanorods. Moreover, the reduction and oxidation peaks shift to comparatively lower and higher applied potentials, respectively, with a rise in scanning rate, representing the battery-type behavior. The NiO nanorods delivered a C_S (calculated from eqn (S2)†) of 368 F g^{-1} and 177.9 F g^{-1} at scanning rates of 5 and 100 mV s^{-1}, respectively. Due to the porous character of the NiO nanorods, which facilitates faultless transport of electrons and diffusion of OH^- ion, the larger C_S at a slower scan rate can be credited to their significant available surface-area. The OH^- ions diffusion is significantly hampered at higher scan rates, which results in lower *C*s. Furthermore, the correlation between the scan rate (υ) and peak J (i_p), as shown in Fig. 6(b), provides support for both the diffusion and surface charge storage mechanisms in porous NiO nanorods. GCD investigations at different J running from 0.5 to 5 A g^{-1} were utilized to further validate the bidirectional energy storage process (Fig. 6(c)). The C_S values of the mesoporous NiO nanorods, dependent on J (Fig. 6(d)), were calculated using eqn (S4).† When the J was increased to 5 A g^{-1} from 0.5 A g^{-1}, a C_S of 350.5 F g^{-1} slowly decreased to 263.8 F g^{-1}. Understanding the long-term reliability of the supercapacitor strongly depends on the cyclability of electrodes for the anodic

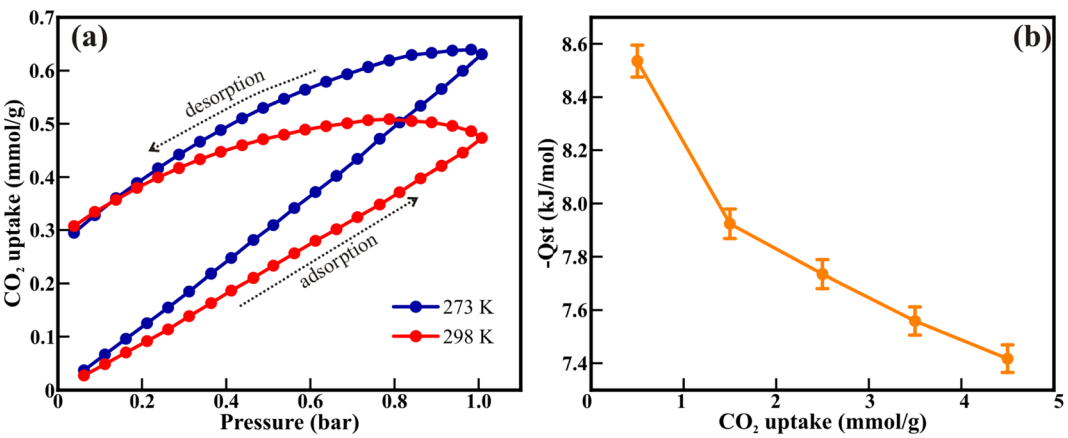

Fig. 5 (a) The CO_2 adsorption–desorption isotherm at 273 and 298 K, and (b) associated isosteric heat calculated from the Clausius–Clapeyron equation.

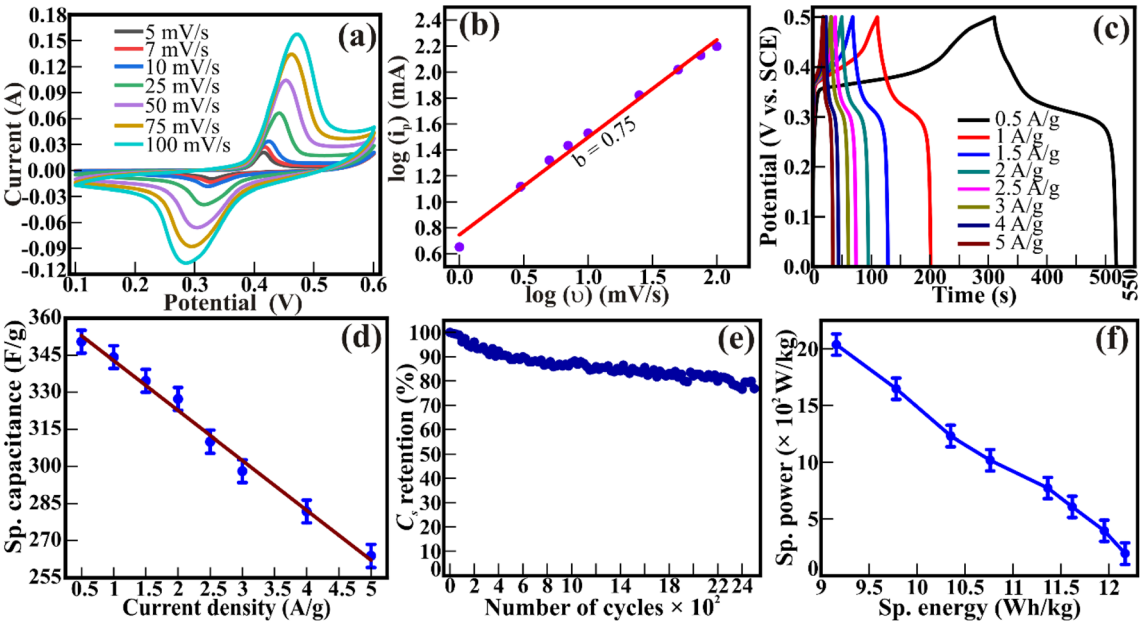

Fig. 6 (a) CV curves for porous NiO nanorods at several scanning rates. (b) The cathodic peak current density variation with scan rate. (c) GCD curves and (d) specific capacitance determined at various current densities; (e) capacitance retention at 1 A g^{-1}; and (f) Ragone plot of porous NiO nanorods.

process. At J of 1 A g^{-1}, following 2500 repeated discharging and charging cycles, ~76.8% retention of the initial capacitance is observed, indicating the stability of NiO nanorods (Fig. 6(e)). The specific energy and power of NiO nanorods (Fig. 6(f)) were evaluated to assess their overall electrochemical performance. The NiO nanorods demonstrated maximum specific energy of 12.17 W h kg^{-1} at a specific power of 193.68 W kg^{-1} and maximum specific power of 2035.49 W kg^{-1} at a specific energy of 9.15 W h kg^{-1}. These considerable power and energy density values result from the porous nanorods formed by the well-connected NiO nanoparticles, which have a large number of readily accessible activation sites and a vast surface area.

The OER activity of the porous NiO nanorods was evaluated from the linear sweep voltammetry (LSV) plots using 1 M KOH as an electrolyte, as shown in Fig. 7(a). In contrast to the IrO_2 reference catalyst, which had an overpotential of 354 ± 4 mV,

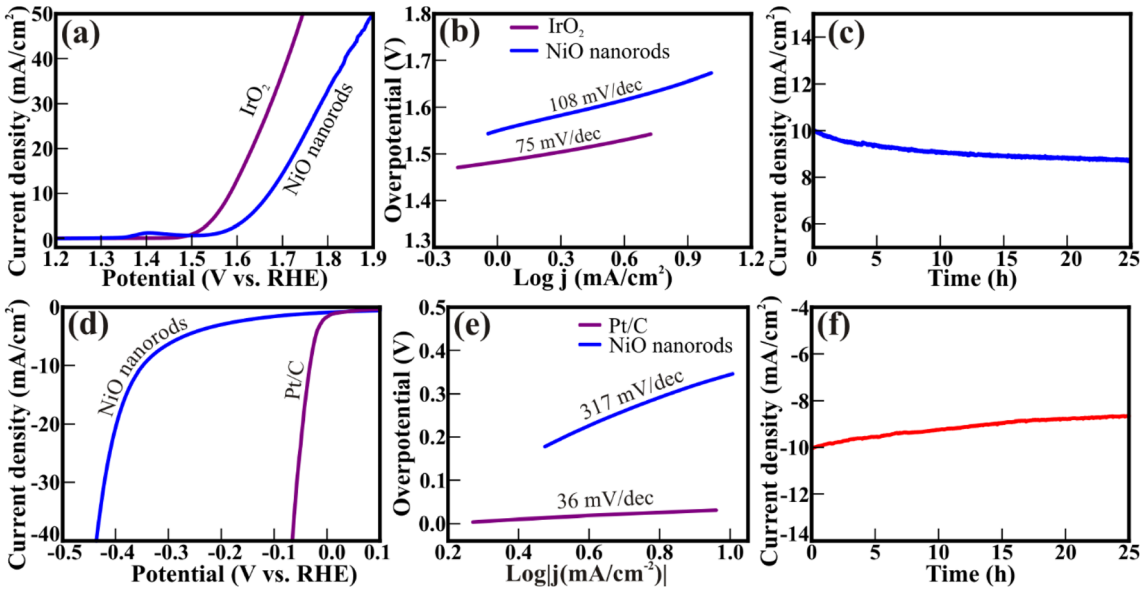

Fig. 7 (a) A polarisation curve (LSV plots), (b) corresponding Tafel plot. (c) Chronoamperometric (CA) stability test at a 441 mV applied overpotential for 25 h in 1 M KOH of porous NiO nanorods towards the OER activity. (d) Polarization curve (LSV plot), (e) associated Tafel plot, and (f) chronoamperometric stability test at a 345 mV applied overpotential for 25 h in 0.5 M H_2SO_4 of porous NiO nanorods for HER activity.

the porous NiO nanorods displayed an overpotential of 441 ± 6 mV to gain a J of 10 mA cm^{-2}. Additionally, the surge in J at a potential of >1.35 V (*vs.* RHE) demonstrates the presence of numerous functional exchanges between Ni^{2+} and Ni^{3+}, which contribute to increased OER activity and are consistent with the XPS analysis. The related Tafel plots (Fig. 7(b)) revealed that the IrO_2 reference catalyst and NiO nanorods had a Tafel slope of 108 ± 3 and 75 ± 2 mV dec^{-1}, respectively. Similar catalytic rates and reaction kinetics towards OER activity is indicated by the closeness of the Tafel slopes of the NiO nanorods and reference IrO_2 catalyst. The reliability of the electrocatalyst was analyzed by performing a CA stability test for 25 h at an overpotential of 441 mV (Fig. 7(c)). The J maintains good stability for 25 hours at 8.73 mA cm^{-2} (13.03% loss). Consecutive LSV cycles were also used to examine the long-term reliability (Fig. S1, ESI†). After 3000 successive LSV cycles, a modest increase in overpotential of 11 mV for NiO nanorods confirms their better stability for OER activity.

Furthermore, the HER activity of NiO nanorods was evaluated from LSV plots (Fig. 7(d)) using 0.5 M H_2SO_4 as an electrolyte. An overpotential of 345 ± 4 mV and 32 ± 3 mV was estimated for the NiO nanorods and reference Pt/C electrocatalysts, respectively, in achieving J of 10 mA cm^{-2}. The correlated Tafel plots (Fig. 7(e)) revealed a Tafel slope of 317 ± 4 and 36 ± 2 mV dec^{-1} for NiO nanorods and Pt/C electrocatalysts, respectively. To assess how well the NiO nanorods perform in terms of HER activity, a stability test was carried out at a 345 mV overpotential (Fig. 7(f)). After 25 h stability assessment, the J decreased over time and eventually reached 8.65 mA cm^{-2} (around 13.8% loss), showing relatively consistent HER activity. The continuous LSV cycles were also used to determine the long-term durability of the NiO nanorods. After 3000 repeated LSV cycles, 12.5 mV rise in overpotential at a J of 10 mA cm^{-2} showcased the remarkable durability of the particulate porous NiO nanorods towards HER activity in an acidic solution (Fig. S2, ESI†). Overall, nanoparticulate porous 1D NiO nanorods showed good potential to produce hydrogen and oxygen through water electrolysis (Table 1).

Furthermore, the chemical characteristics, crystal structure, and morphological features were examined from EDS, XRD, and FESEM to demonstrate the stability of the NiO nanorods post electrocatalytic reactions. After uninterrupted assessments of the stability test (CA) for 25 h in a basic solution, the Rietveld refinement of the X-ray diffractograms of the NiO nanorods (Fig. 8(a)) shows the reflected and analyzed patterns, Bragg's positions, and difference curves for the space group $Fm\bar{3}m$ (ICSD No. 9008693) and $P63/m$ (14-0481), akin to that of before the stability study. The reasonably good fit of the diffraction peaks at 2θ = 37.33°, 43.38°, 63.03°, 75.60°, and 79.61° represents the (111), (020), (022), (131), and (222) peaks, respectively, representing the existence of the cubic NiO phase with cell volume (V) of 72.77 cm^3 g^{-1} and lattice parameters (*i.e.*, $a = b = c$) of 4.174 Å. Other minor peaks observed at 2θ = 24.4°, 28.05°, and 31.9° correspond to the (010), (011), and (002) crystal planes, indicating the existence of the Ni_2O_3 phase with the cell volume (V) for 102.80 cm^3 g^{-1} and lattice parameters of 4.573 Å ($\equiv a = b$) and 5.649 Å ($\equiv c$). The values of the fitting parameters, namely R_f (R-factor) and GoF (goodness of fit), are 1.90 and 2.83, respectively. Moreover, the amount of NiO and Ni_2O_3 remained similar as before the stability study. The morphology of the NiO nanorods also remained identical to those of the synthesized samples, even after the uninterrupted CA assessments for 25 h (Fig. 8(b)). In addition, the EDS spectra exhibit individual peaks (Fig. 8(c)), demonstrating that Ni and O were present following the electrocatalytic reactions without any additional foreign elements. The C is observed due to the use of carbon tape during the EDS measurement. This indicated that even after a 25 h electrocatalytic reaction, the NiO nanorods displayed remarkable structural, morphological, and chemical robustness against the water-splitting activity.

An investigation using electrochemical impedance spectroscopy (EIS) was conducted to probe the charge transfer pathway during OER activity (Fig. 9). The electrocatalyst and electrolyte contact exhibits an interfacial resistance (R_s) of 9.26 Ω. Moreover, the resistance at the textural boundary (R_{ct1}) and the core/bulk of NiO nanorods (R_{ct2}) are 28.9 and 102 Ω, respectively, indicating the active contributions of both the textural boundaries and core

Table 1 Comparative performance of various NiO nanostructures towards OER and HER activity

	Overpotential (mV) @ 10 mA cm^{-2}		Tafel slope (mV dec^{-1})		
Catalyst	OER	HER	OER	HER	Ref.
1D NiO nanoparticulate porous nanorods	441	345	108	317	This work
Ni/NiO@rGO	480	582	41	63	31
NiO hollow microsphere	370	424	156	105	20
Ni–NiO@3D graphene	1640	310	55	78	33
NiO nanoparticles/GO	453	625	—	—	32
MoS_2@NiO nanocomposite	—	406	—	44	34
Er_2O_3/Ni–NiO	—	39	—	71.2	38
CeO_2/Ni–NiO	—	42	—	103.1	
LaO_X/Ni–NiO	—	45	—	137.9	
GdO_X/Ni–NiO	—	47	—	101.1	
NdO_X/Ni–NiO	—	52	—	122.9	
YO_X/Ni–NiO	—	58	—	107.3	
Ni–NiO	—	84	—	145.5	

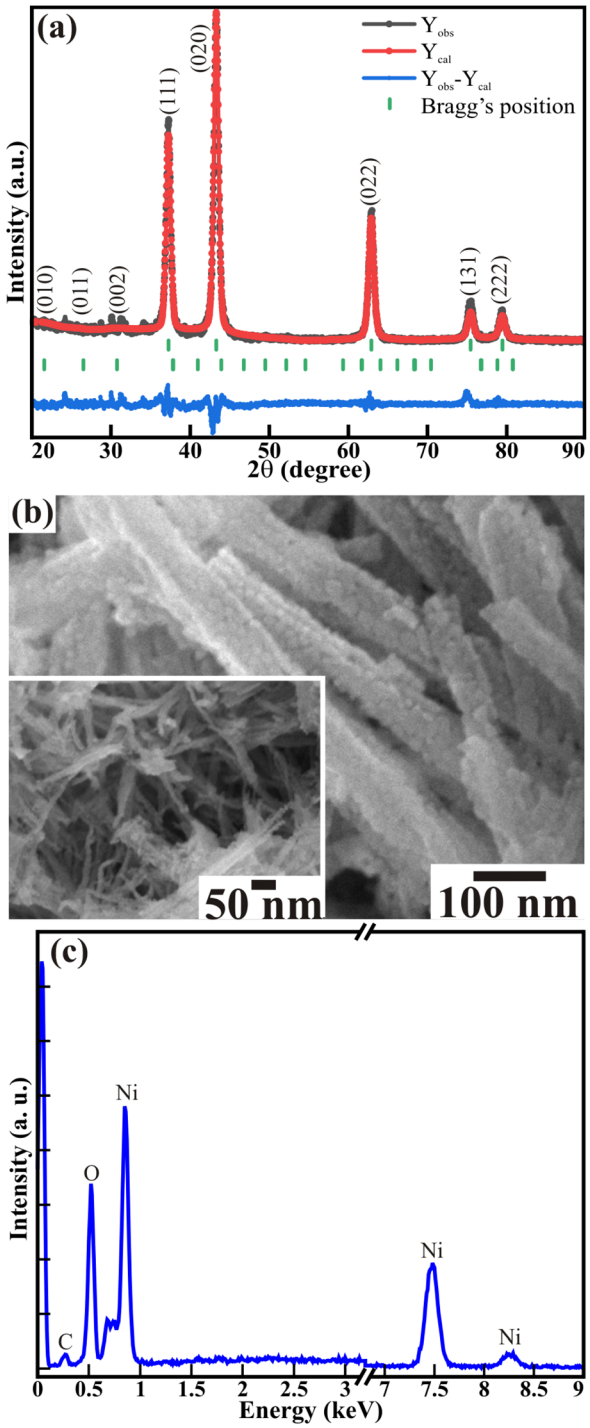

Fig. 8 (a) XRD, (b) FESEM, and (c) EDS analysis of the NiO nanorods after undergoing a CA test for 25 h in a basic medium.

of the NiO nanoparticles in the electrocatalytic OER activities. The R_{ct1} and R_{ct2} of the porous 1D nanorods are comparable to those of the 0D NiO nanoparticles of similar size (<10 nm) reported in our previous study.[36] Furthermore, the electrochemically active surface area (ECSA) and double layer capacitance (C_{dl}) of the porous NiO nanorods are determined from CV curves (Fig. S3(a), ESI†) and the corresponding plot of $\Delta J/2$ *vs.* scan rate (Fig. S3(b), ESI†). The estimated C_{dl} of 0.623 ± 0.031 mF cm^{-2} for the

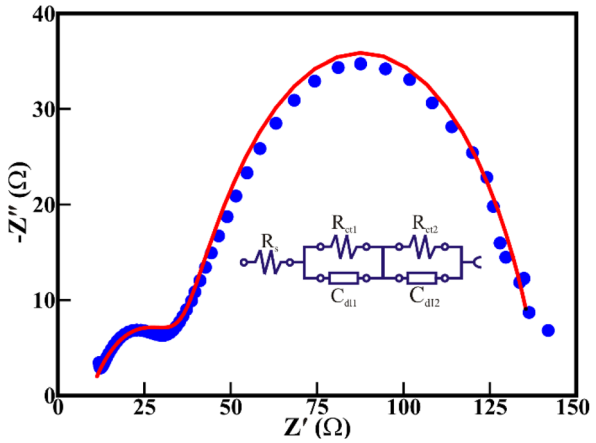

Fig. 9 Electrochemical impedance spectrum of the NiO nanorod electrocatalyst at an overpotential of 441 mV towards OER activity.

particulate porous NiO nanorods illustrates the ECSA of 15.57 cm^2. This implies that highly porous NiO nanorods made of interlinked NiO nanoparticles provide more open active sites, hence administering enhanced electrochemical and adsorption activity.

Conclusions

In conclusion, we have hydrothermally synthesized porous NiO nanorods formed by interconnecting cubic crystalline NiO nanoparticles with the $Fm\bar{3}m$ space group. The surface morphological and structural analysis confirm the assembly of porous NiO nanorods of diameter ~47.12 nm due to the interlinking of nanoparticles of diameter ~13 nm, providing a surface-to-volume ratio of 0.0279/Å, surface-area of 84.731 m^2 g^{-1} and a mean pore diameter of 3.74 nm. The high-resolution XPS and EXAF confirm the existence of Ni^{2+}/Ni^{3+} transitions and 2+ octahedron coordination in the NiO nanorods. A good regenerative CO_2 capturing ability with CO_2 uptake of 0.63 mmol g^{-1} at 273 K and the competent electrochemical energy storage ability with good retention (*i.e.*, 76.84% @ 2500 cycles), specific energy (*i.e.*, 12.17 W h kg^{-1} at 0.5 A g^{-1}) and specific power (*i.e.*, 2035.49 W kg^{-1} at 5 A g^{-1}) indicate the potentials of the porous NiO nanorods as electrode materials for CO_2 capture and electrochemical supercapacitor. The porous nature increased the surface-area and, consequently, the electro-catalytically active surface sites in the NiO nanorods, therefore, delivered overpotentials of 345 and 441 mV for the HER and OER activities, respectively, and demonstrated the long-lasting stability of NiO nanorods in both acidic and basic media for total water-electrolysis. Overall, this study suggests that similar to nanoparticulate porous NiO nanorods, stable materials that offer hetero-architectural porous frameworks with a greater surface area and readily accessible active sites may be candidates for multifunctional devices.

Conflicts of interest

There are no conflicts to declare.

Acknowledgements

The authors would like to thank and acknowledge SERB-DST and TARE-DST under grant no. CRG/2022/000160 and TAR/2019/000106, respectively, for the financial support to this research work. R. B. is thankful to the DST for providing the INSPIRE fellowship for the PhD program [IF190052].

References

1 R. S. Devan, R. A. Patil, J.-H. Lin and Y.-R. Ma, *Adv. Funct. Mater.*, 2012, **22**, 3326–3370.
2 Y. Bao and F. Zhang, *Small Structures*, 2022, **3**, 2100226.
3 S. S. Cheema, N. Shanker, L.-C. Wang, C.-H. Hsu, S.-L. Hsu, Y.-H. Liao, M. San Jose, J. Gomez, W. Chakraborty, W. Li, J.-H. Bae, S. K. Volkman, D. Kwon, Y. Rho, G. Pinelli, R. Rastogi, D. Pipitone, C. Stull, M. Cook, B. Tyrrell, V. A. Stoica, Z. Zhang, J. W. Freeland, C. J. Tassone, A. Mehta, G. Saheli, D. Thompson, D. I. Suh, W.-T. Koo, K.-J. Nam, D. J. Jung, W.-B. Song, C.-H. Lin, S. Nam, J. Heo, N. Parihar, C. P. Grigoropoulos, P. Shafer, P. Fay, R. Ramesh, S. Mahapatra, J. Ciston, S. Datta, M. Mohamed, C. Hu and S. Salahuddin, *Nature*, 2022, **604**, 65–71.
4 X.-P. Zhai, L.-F. Gao, H. Zhang, Y. Peng, X.-D. Zhang, Q. Wang and H.-L. Zhang, *ACS Appl. Nano Mater.*, 2022, **5**, 1169–1177.
5 Y. Wang, Y. Liu, J. Tong, X. Shi, L. Huang, Z. Xiao, G. Wang and D. Pan, *Sol. Energy Mater. Sol. Cells*, 2022, **236**, 111511.
6 V. Manjunath, S. Bimli, K. H. Parmar, P. M. Shirage and R. S. Devan, *Sol. Energy*, 2019, **193**, 387–394.
7 R. Mandavkar, R. Kulkarni, S. Lin, S. Pandit, S. Burse, M. Ahasan Habib, P. Pandey, S. Hee Kim, M.-Y. Li, S. Kunwar and J. Lee, *Appl. Surf. Sci.*, 2022, **574**, 151739.
8 V. Manjunath, P. K. Mishra, R. Dobhal, S. Bimli, P. M. Shirage, S. Sen, P. A. Shaikh and R. S. Devan, *ACS Appl. Electron. Mater.*, 2021, **3**, 4548–4557.
9 N. Kitchamsetti, M. Samtham, P. N. Didwal, D. Kumar, D. Singh, S. Bimli, P. R. Chikate, D. A. Basha, S. Kumar, C.-J. Park, S. Chakraborty and R. S. Devan, *J. Power Sources*, 2022, **538**, 231525.
10 Z. Feng, Y. Zhang, J. Sun, Y. Liu, H. Jiang, M. Cui, T. Hu and C. Meng, *Chem. Eng. J.*, 2022, **433**, 133795.
11 Q. Li, W. Zeng and Y. Li, *Sens. Actuators B: Chem.*, 2022, **359**, 131579.
12 K. H. Parmar, V. Manjunath, S. Bimli, P. R. Chikate, R. A. Patil, Y.-R. Ma and R. S. Devan, *Chinese J. Phys.*, 2022, **77**, 143–150.
13 R. Eivazzadeh-Keihan, E. Bahojb Noruzi, E. Chidar, M. Jafari, F. Davoodi, A. Kashtiaray, M. Ghafori Gorab, S. Masoud Hashemi, S. Javanshir, R. Ahangari Cohan, A. Maleki and M. Mahdavi, *Chem. Eng. J.*, 2022, **442**, 136183.
14 F. Yuan, Y. Xia, Q. Lu, Q. Xu, Y. Shu and X. Hu, *Talanta*, 2022, **244**, 123419.
15 Z. Wang, Z. Lin, Y. Wang, S. Shen, Q. Zhang, J. Wang and W. Zhong, *Adv. Mater.*, 2023, 2302007.
16 L. Lu, H. Zheng, Y. Li, Y. Zhou and B. Fang, *Chem. Eng. J.*, 2023, **451**, 138668.
17 G. Liu, F. Hou, X. Wang and B. Fang, *Appl. Surf. Sci.*, 2023, **615**, 156333.
18 G. Liu, F. Hou, X. Wang and B. Fang, *Materials*, 2022, **15**, 7602.
19 Y. Miao, X. Zhang, Y. Sui, E. Hu, J. Qi, F. Wei, Q. Meng, Y. He, Z. Sun, Y. Ren and Z. Zhan, *Mater. Lett.*, 2022, **265**, 127300.
20 N. Kitchamsetti, P. R. Chikate, R. A. Patil, Y.-R. Ma, P. M. Shirage and R. S. Devan, *CrystEngComm*, 2019, **21**, 7130–7140.
21 Y. Lei, T. Xu, S. Ye, L. Zheng, P. Liao, W. Xiong, J. Hu, Y. Wang, J. Wang, X. Ren, C. He, Q. Zhang, J. Liu and X. Sun, *Appl. Catal., B*, 2021, **285**, 119809.
22 T. J. Macdonald, J. Xu, S. Elmas, Y. J. Mange, W. M. Skinner, H. Xu and T. Nann, *Nanomaterials*, 2014, **4**, 256–266.
23 K. Han, H. Huang, Q. Gong, T. Si, Z. Zhang and G. Zhou, *J. Mater. Sci.*, 2018, **53**, 12477–12491.
24 Y.-z. Zheng, H.-y. Ding and M.-l. Zhang, *Mater. Res. Bull.*, 2009, **44**, 403–407.
25 X.-M. Liu, X.-G. Zhang and S.-Y. Fu, *Mater. Res. Bull.*, 2006, **41**, 620–627.
26 D. Wang, Q. Wang and T. Wang, *Ionics*, 2013, **19**, 559–570.
27 H. Pang, Q. Lu, Y. Zhang, Y. Li and F. Gao, *Nanoscale*, 2010, **2**, 920–922.
28 S. Ci, Z. Wen, Y. Qian, S. Mao, S. Cui and J. Chen, *Sci. Rep.*, 2015, **5**, 11919.
29 H. Pang, B. Guan, W. Sun and Y. Wang, *Electrochim. Acta*, 2016, **213**, 351–357.
30 A. Mondal, A. Paul, D. N. Srivastava and A. B. Panda, *Int. J. Hydrog. Energy.*, 2018, **43**, 21665–21674.
31 S. S. Narwade, S. M. Mali, R. V. Digraskar, V. S. Sapner and B. R. Sathe, *Int. J. Hydrog. Energy.*, 2019, **44**, 27001–27009.
32 S. G. Jo, C.-S. Kim, S. J. Kim and J. W. Lee, *Nanomaterials*, 2021, **11**, 3379.
33 N. Ullah, W. Zhao, X. Lu, C. J. Oluigbo, S. A. Shah, M. Zhang, J. Xie and Y. Xu, *Electrochim. Acta*, 2019, **298**, 163–171.
34 A. Q. Mugheri, S. Ali, G. S. Narejo, A. A. Otho, R. Lal, M. A. Abro, S. H. Memon and F. Abbasi, *Int. J. Hydrog. Energy.*, 2020, **45**, 21502–21511.
35 G. Liu, F. Hou, S. Peng, X. Wang and B. Fang, *Nanomaterials*, 2022, **12**, 2935.
36 V. Manjunath, S. Bimli, R. Biswas, P. N. Didwal, K. K. Haldar, M. Mahajan, N. G. Deshpande, P. A. Bhobe and R. S. Devan, *Int. J. Hydrog. Energy*, 2022, **47**, 39018–39029.
37 N. Kitchamsetti, M. S. Ramteke, S. R. Rondiya, S. R. Mulani, M. S. Patil, R. W. Cross, N. Y. Dzade and R. S. Devan, *J. Alloys Compd.*, 2021, **855**, 157337.
38 W. Sha, Y. Song, P. Liu, J. Wang, B. Xu, X. Feng and J. Guo, *ChemCatChem*, 2022, **14**, e202101975.